

Diffusive and capillary instabilities of viscous fluid threads in microchannels

Thomas Cubaud ^{*}, Bryan Conry , Xiaoyi Hu , and Thai Dinh 

Department of Mechanical Engineering, Stony Brook University, New York 11794, USA



(Received 7 June 2021; accepted 19 August 2021; published 7 September 2021)

We experimentally examine the formation of viscous fluid threads in hydrodynamic focusing sections using both miscible and immiscible fluid pairs at relatively low flow rates. A systematic comparative study is conducted between diffusive and capillary regimes using a viscous oil and a variety of polar organic solvents in a simple microflow geometry. Silicone oil and various low molecular weight alcohols are used as model fluids to investigate the dynamics of viscous multiphase flows at ultralow interfacial tension and with partially miscible systems. An original methodology based on analysis of thread width and detachment length in the viscous regime is developed to quantify various interfacial destabilization processes over a wide range of injection flow rates. For miscible fluid pairs, we investigate several regimes of thread swelling and, for immiscible fluid pairs, we discuss diverse modes of droplet formation and wetting dynamics. This work provides a comprehensive general classification of immiscible and miscible fluid dynamics with large viscosity contrasts in microchannels together with a unifying phenomenological description of thread behavior based on simple functional relationships to better delineate the role of flow parameters and fluid properties on viscous microflow processes.

DOI: [10.1103/PhysRevFluids.6.094202](https://doi.org/10.1103/PhysRevFluids.6.094202)

I. INTRODUCTION

Flows of physical and industrial interest often result from the chemical nature of their components. The term “oil” typically refers to a substance that does not mix with water due to lack of chemical affinity and a simple classification consists in sorting fluids as polar, such as water, or nonpolar, such as oils. In practice, many oils are made of long molecules and display complex rheological and interfacial behaviors [1–3]. Their usually large viscosity coefficients make them thick and sticky, and for ease of manipulation, it is often desirable to reduce their overall viscosity through mixing with a miscible thinner or through emulsification with a low-viscosity immiscible fluid phase [4]. Alcohols comprise a broad class of polar organic compounds that find use in a myriad of situations, such as disinfectants and antiseptics, solvents and precursors, and as direct fuel or fuel additive [5]. Primary alcohols also exhibit various degrees of solubility, i.e., partial miscibility, with both water and oils depending on molecular weight and structure due to their hydrophobic alkyl chain and hydrophilic hydroxyl group [6]. As a result, alcohols are sometimes used as cosurfactant in the formulation of microemulsions [7] and their inclusion in oil and water systems can lead to intriguing spontaneous emulsification phenomena [8–11]. Therefore, oil-alcohol multiphase flows present important industrial and scientific potentials; however, systematic studies of flow interactions between oil and alcohol fluid pairs are limited [12] and the phenomenology associated with highly viscous multifluid microflows having ultralow interfacial tension or with partial miscibility has remained relatively unexplored to date.

Microfluidic platforms offer significant advantages to examine the flow interplay between dissimilar fluids at the small scale [13–16]. Precise control of microgeometries enables fabrication

^{*}thomas.cubaud@stonybrook.edu

of miniature flow contactors that are ideal for studying the spatiotemporal evolution of fluid interfacial regions using high-magnification and high-speed imaging systems [17–22]. In addition, the reduced amount of fluids required for examining flows in microchannels permits systematic studies of homologous fluid series with fast screening and high throughput over a broad range of flow rates. As a result, microchannels have been employed to investigate the formation of a variety of fluid elements, including droplets, bubbles, and threads [23–28] with applications ranging from nanoparticle synthesis to microfiber fabrication [29–31]. Hydrodynamic instabilities can also be finely manipulated to enhance micromixing and structure complex fluids in microgeometries depending on fluid properties [32–35]. When fluids have a large difference in viscosity, transport of thick fluids in pipes can also be facilitated through the formation of core-annular flows where a thin fluid is essentially employed as a lubricant for a central viscous thread [36–40]. Our previous work has shown the possibility to form locally stable microfluidic threads, which destabilize at low flow rates in the form of swollen or buckled threads when fluids are miscible [41] or into droplets when fluids are immiscible [42]. Hence, viscous threads can be employed to interrogate the role of individual and mutual fluid properties on interfacial fluid dynamics and further investigate analogies in the flow behavior of miscible and immiscible fluid pairs, which are sometimes compared in the context of Korteweg theory [43–47]. Microfluidic control of fluids’ contact area using continuous flows provides a practical mean to investigate the role of intermolecular forces on thread behavior; however, a unifying phenomenological description based on simple functional relationships is needed to quantitatively compare the behavior of immiscible and miscible fluid threads.

Here, we experimentally probe the flow behavior of viscous oil threads in a variety of primary and secondary alcohols in hydrodynamic focusing sections. Through broad variations of injection flow rates, we delineate vast flow maps and identify a variety of flow regimes for both miscible and immiscible fluid pairs. We show that functional relationships for thread characteristics, including diameter and detachment length, are similar for both miscible and immiscible fluid pairs in the viscous regime at moderate flow rates. In turn, information gained about the viscous regime is employed as a reference to quantify thread behavior in the diffusive and in the capillary regimes at low flow rates. While our analysis eventually involves dimensionless numbers, including capillary and Péclet numbers, we adopt an original methodology with mathematical formulations of flow characteristics based on absolute and relative flow rates to directly compare dynamics of immiscible and miscible fluid pairs in confined microsystems using a homologous series of alcohol and a silicone oil as model fluid pairs. This unifying approach facilitates interpretation of physical phenomena with clarification of the role of flow parameters and the influence of fluid properties on interfacial fluid dynamics and destabilization processes.

II. EXPERIMENTAL METHODS

In this work, we probe the stability of viscous fluid threads formed through injection of a thick oil $L1$ in a sheath of various polar organic solvents $L2$ using hydrodynamic focusing sections with square microchannels of width $h = 250 \mu\text{m}$. Fluid pairs are composed of diverse low molecular weight alcohols for the external phase and a silicone oil having fixed viscosity $\eta_1 = 96.6 \text{ cP}$ (i.e., 100-cSt oil) for the thread. Such fluid pairs present intriguing properties with a relatively low value of interfacial tension γ_{12} at moderate solvent viscosity η_2 with various degrees of miscibility based on alcohol molecular weight and structure [Fig. 1(a)]. Here, we examine the role of the carbon number n of primary alcohols, ranging from propanol to octanol—together with a few secondary alcohols for low n —on microflow regimes (Table I).

Fluid pairs are labeled based on carbon number and isomer, such as $C3-1$ when $L2$ corresponds to 1-propanol or $C4-2$ when the solvent is 2-butanol. Overall, experiments showed that the four liquid pairs $C3-1$, $C6-1$, $C7-1$, and $C8-1$ are immiscible fluids, while the four liquid pairs $C3-2$, $C4-1$, $C4-2$, and $C5-1$ are miscible fluids. The value of interfacial tension γ_{12} for immiscible fluid pairs is determined using a Du Nouy ring tensiometer, expected for the case of 1-Propanol, where the very low value of γ_{12} is directly estimated in this work through examination of the dripping regime.

TABLE I. Properties of inner fluid $L1$ and outer fluid $L2$ with corresponding dynamic viscosities η_1 and η_2 , viscosity contrast $\chi = \eta_1/\eta_2$, interfacial tension γ_{12} , and diffusion coefficient D_{12} .

Fluid pair	$L1$	η_1 (cP)	$L2$	η_2 (cP)	χ	γ_{12} (mN/m)	D_{12} (m ² /s)
C3-1	Silicone oil	96.6	1-Propanol	2.1	47	0.1	–
C3-2			2-Propanol	2.3	43	–	3.5×10^{-10}
C4-1			1-Butanol	2.8	34	–	2.5×10^{-10}
C4-2			2-Butanol	3.6	27	–	1.6×10^{-10}
C5-1			1-Pentanol	3.6	27	–	1.5×10^{-10}
C6-1			1-Hexanol	4.8	20	0.18	–
C7-1			1-Heptanol	6.3	15	0.31	–
C8-1			1-Octanol	8.3	12	0.76	–

For miscible fluid pairs, the coefficient of diffusion D_{12} is determined based on analysis of diffusive thread behavior [12] and interfacial tension γ_{12} is considered negligible. Indeed, while the solvent viscosity η_2 displays monotonic behavior with the carbon number n of primary alcohols [Fig. 1(b), inset], interfacial tension γ_{12} vanishes for miscible fluid pairs at moderate n . A particularity of the immiscible fluid pairs investigated in this work is their relatively constant characteristic capillary velocity $V^* = \gamma_{12}/\eta_2 \sim 5 \times 10^{-2}$ m/s [Fig. 1(b)]. This characteristic velocity V^* represents the role of fluid properties in the definition of the capillary number $Ca = V/V^*$ [48], where V corresponds to the convective velocity. Hence, beside the difference in γ_{12} and η_2 , fluid pairs flowing at similar velocity V display comparable capillary numbers Ca . By contrast, using our simplified analytical framework where $\gamma_{12} \sim 0$ for miscible fluids yields a negligible $V^* \sim 0$ for diffusive fluid pairs. In this case, the Péclet number $Pe = Vh/D_{12}$, where h is the channel width, is employed to characterize flow regimes and consists in the ratio of convective velocity V to characteristic diffusive velocity D_{12}/h . The convective velocity V is typically defined as the total superficial velocity $J_T = (Q_1 + Q_2)/h^2$, where Q_1 is the volume flow rate of fluid $L1$ injected from the central channel and Q_2 is the total flow rate of fluid $L2$ introduced in the side channels. In general, however, as wide differences in stream velocities can arise due to viscosity contrasts in stratified microflows [15], flow maps are based on flow rates Q_1 and Q_2 instead of superficial velocities. To compare various regimes across multiple fluid pairs, we employ orthogonal hydrodynamic focusing sections where the oil $L1$ is injected in the central channel and the solvent $L2$ is symmetrically injected from the side channels [Fig. 1(c)]. Chemically resistant microdevices are fabricated in silicon and glass using standard microfabrication techniques [49] and microfluidic platforms are placed on top of an

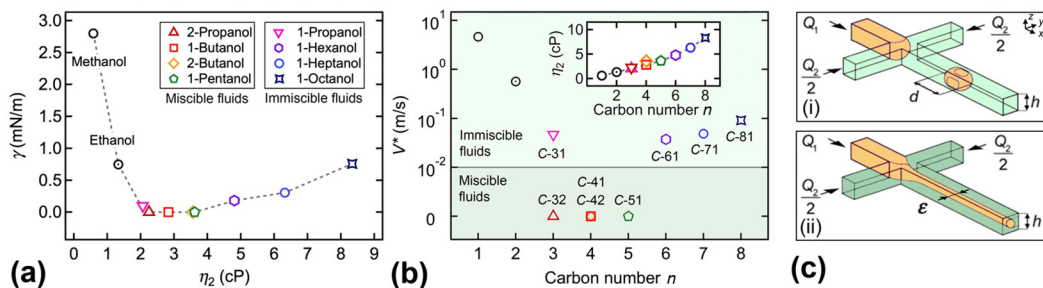


FIG. 1. Fluid properties. (a) Evolution of interfacial tension γ_{12} between silicone oil and alcohol as a function of alcohol viscosity η_2 . (b) Characteristic capillary velocity $V^* = \gamma_{12}/\eta_2$ of fluid pairs. Inset: solvent viscosity η_2 as a function of carbon number. (c) Schematics of square hydrodynamic focusing section where a viscous fluid $L1$ is centrally injected at Q_1 and a solvent $L2$ is symmetrically introduced at Q_2 resulting in various regimes, including (i) dripping droplet, and (ii) viscous thread.

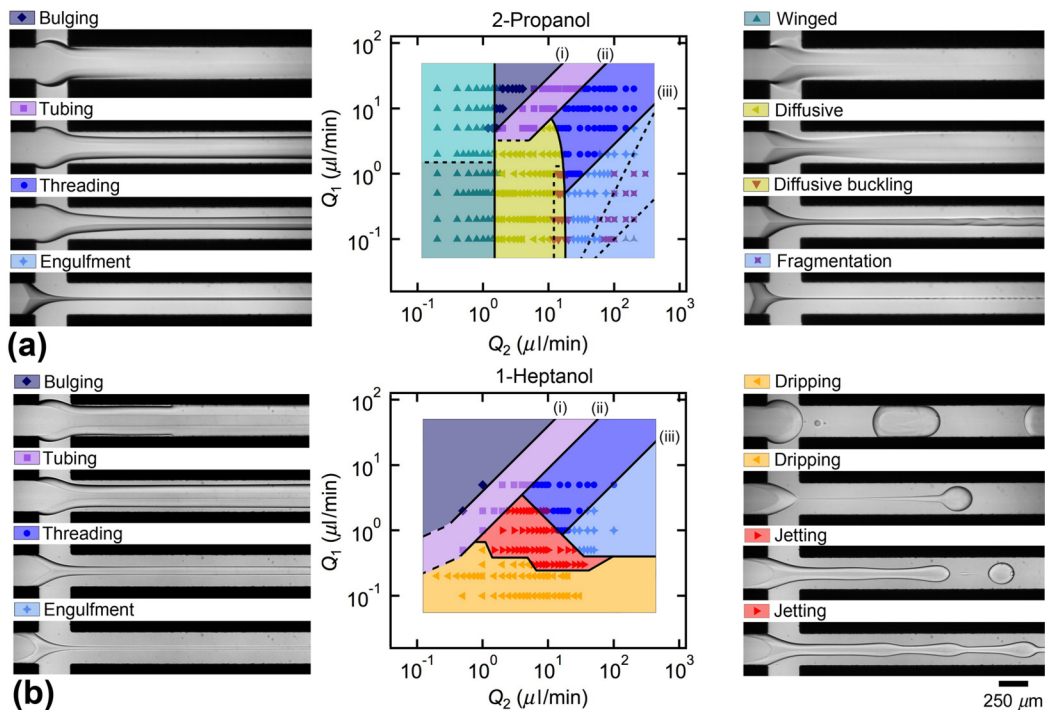


FIG. 2. Maps of flow regimes for miscible and immiscible fluid pairs with characteristic micrographs. Flow rates (Q_1 , Q_2) in $\mu\text{l}/\text{min}$. (a) Miscible fluid pair *C3-2* (*L2*: 2-propanol). Structural flow regimes: bulging (5, 2), tubing (10, 10), threading (20, 40), and engulfment (1, 90). Unstable flow regimes: winged (0.5, 1.2), diffusive (0.5, 5), diffusive buckling (0.5, 20), and fragmentation (0.5, 200). (b) Immiscible fluid pair *C7-1* (*L2*: 1-heptanol). Structural flow regimes: bulging (5, 1), tubing (5, 3), threading (5, 40), and engulfment (0.5, 45). Destabilizing flow regimes: dripping (0.2, 0.5), dripping tail (0.2, 9), jetting (0.3, 7), and jetting beads (0.3, 9). Base flow regime transitions at constant φ : (i) bulging-tubing, (ii) tubing-threading, (iii) threading-engulfment.

inverted microscope equipped with a high-speed camera for flow diagnostics. We use high-pressure syringe pumps to drive fluids into microchannels that are square in cross section with constant width $h = 250 \mu\text{m}$. Using this method, one would expect the continuous formation of droplets of size d when the fluids are immiscible and core-annular flows of diameter ε when the fluids are miscible fluids. In the following, however, we reveal a variety of flow regimes as well as refine flow classification and quantitatively compare the role of fluid properties on viscous microflow phenomena.

III. GENERAL FLOW CLASSIFICATION

Microfluidic multiphase flows display a wide variety of flow patterns depending on fluid properties, flow parameters, and local geometries. Here, the systematic use of an orthogonal hydrodynamic focusing section with square microchannels provides a basis for the comparative study of the role of individual and mutual fluid properties on flow morphologies using both miscible and immiscible fluids. For a given fluid pair, injection flow rates are varied over multiple orders of magnitude to cover large maps in the (Q_1, Q_2) -parameter space where flow regimes are sorted using various symbols and colors to facilitate broad overview and analysis (Fig. 2). While regime classification is based on specific features of flow morphologies, many flow transitions are progressive with a smooth evolution of multiphase flow properties. Therefore, criteria for regime definition are developed based on quantities that are measurable across flow regimes to provide a useful reference

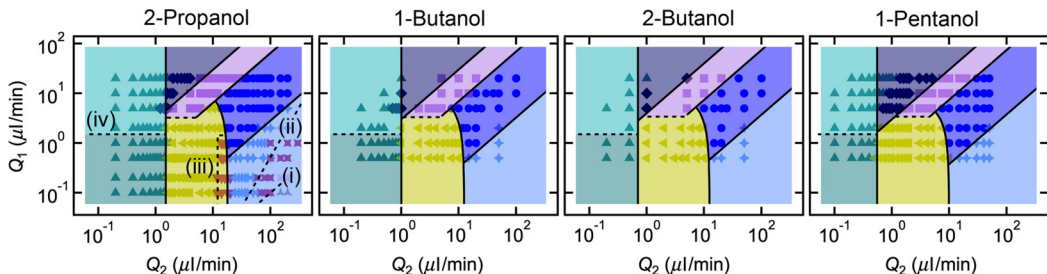


FIG. 3. Flow maps of miscible fluid pairs, C3-2 (2-propanol), C4-1 (1-butanol), C4-2 (2-butanol), and C5-1 (1-pentanol), including structural regimes, such as threading (●), tubing (■), engulfment (◆), and bulging (◆), and unstable regimes, such as diffusive (◄), diffusive buckling (▼), winged (▲), fragmentation (✕), and limiting (▲). See main text for subregime transition lines (i)–(iv).

and comparison in the elaboration of a universal flow classification of viscous fluid threads in symmetrical hydrodynamic focusing sections. In particular, it is instructive to define a viscous regime when the fluid $L1$ forms a straight, central stream of width ε near the junction in the square channel. In our case of large viscosity ratios $\chi = \eta_1/\eta_2 \gg 1$, the viscous fluid $L1$ progressively detaches from the top and bottom walls to form a lubricated thread. The various degrees of thread ensheathing with fluid $L2$ lead to the definition of base flow regimes, including fully lubricated threads with the engulfment and threading regimes at low $\varphi = Q_1/Q_2$, partial side lubrication and contact with top and bottom walls in the tubing regime at moderate φ , and $L1$ contact with four walls with gutter flow of $L2$ in the bulging regime at large φ . In practice, viscous regimes are found at moderate $Q_T = Q_1 + Q_2$, i.e., in the upper right region of flow maps, for both miscible and immiscible fluid pairs (Fig. 2). Basic thread lubrication transitions occur at fixed φ for a given χ and are labeled with (i) for the bulging-tubing transition, (ii) for the tubing-threading transition, and (iii) for the threading-engulfment transition in Fig. 2. By contrast, interfacial properties play an important role at low Q_T , i.e., in the bottom left region of flow maps, with the presence of diffusive regimes for miscible fluids [Fig. 2(a)] and capillary regimes for immiscible fluids [Fig. 2(b)]. Other flow patterns, including inertial and gravitational regimes [41], are typically found at high Q_T and large h and are beyond the scope of this current work, albeit observation of small miscible thread fragmentation at large Q_2 suggests the presence of inertial instabilities as discussed in the next section. Overall, focus here is on the influence of fluid properties on thread dynamics at relatively low flow rates with examination of outer regions of flow maps at very low flow rates. Data show that the viscous regime constitutes a basic structural regime and provides a useful basis for refining analysis of diffusive and capillary regimes. Hence, we adopt the terminology of capillary and diffusive instabilities to describe significant deviations from the viscous regimes at low flow rates near the fluid junction. While such classification is useful to describe flow behavior in short microfluidic systems, further destabilization of “stable” flow regimes is assumed further downstream as one would expect viscous threads to be always unstable to either capillary or diffusion phenomena in very long microchannels. Here, Fig. 2 enables comparison of initial flow regimes between miscible and immiscible fluid pairs at large viscosity contrasts. In the following, we examine flow maps and subregimes in greater detail and provide quantitative analysis of the evolution of multiphase flow properties across flow patterns.

IV. DIFFUSIVE THREADS

A. Flow maps

We commence our study with flow map analysis of miscible fluid threads (Fig. 3). Structural flow regimes primarily depend on the flow rate ratio $\varphi = Q_1/Q_2$ and viscosity ratio $\chi = \eta_1/\eta_2$. Overall, the use of 100-cSt oil with low molecular alcohols enables modest variations of χ between

12 and 47 with strong disparities of fluid affinity since some fluid pairs are found partially miscible and others are found immiscible. Over wide variations of χ between 10 and 10^4 , previous work with fully miscible silicone oils [41] identified the critical flow rate ratio for the tubing-threading transition in the viscous regime according to $\varphi_{\text{Tub}} = 2\chi^{-0.3}$ and the transition between engulfment and threading regimes according to $\varphi_{\text{Eng}} = 0.27\chi^{-0.6}$. Here, good agreement is found with these correlations for full and partial lubrication transitions of miscible fluid threads as shown in Fig. 3 where lines of constant φ appear oblique on flow maps. The bulging regime consists of a central stream in contact with the four walls of the channels with small streams of $L2$ in the four gutters of the square channel. As a result, the apparent thread size $\varepsilon/h = 1$ and the critical flow rate for the transition remain relatively constant across fluid pairs with $\varphi_{\text{Bulg}} = 3$ given our viscosity ratios. In the focusing section, the central stream appears to bulge in the side channels. We previously labeled this regime as displacement in the context of immiscible fluids [42]. This pattern defines the upper bound of base flow regimes for large φ and corresponds to the more viscous fluid $L1$ entering the inlet channels of fluid $L2$. The other limiting flow regime is found for extremely low $\varphi_{\text{Lim}} = 10^{-3}$, where the low-viscosity fluid $L2$ fully invades the central channel and threads are not readily distinguishable from the sheath flow. This limiting regime is directly observed with fluid pair C3-2 with isopropanol, where the transition φ_{Lim} is indicated with the dashed line (i) in Fig. 3. Flows of similar liquids in focusing sections at low φ can develop complex filamentous structures with the formation of vortices [20,21]. In the case of large χ , experiments with fully miscible silicone oils [41] showed the onset of inertial destabilization of small threads at low φ according to $\varphi_{\text{Ine}} = a\text{Re}$ where $a = b\chi^{-1/2}$ with $b = 3.5 \times 10^{-3}$ and the Reynolds number $\text{Re} = \rho_2 Q_{\text{T}} / (\eta_2 h)$ where ρ_2 is the density of the external phase. Here, over the range of parameters investigated, the largest obtained $\text{Re} \sim 6$ remains relatively modest and the equivalent inertial regime corresponds to the fragmentation pattern as indicated in Fig. 3 for isopropanol with the transition dashed line (ii). Incidentally, the inertial transition yields a scaling of the form $Q_1 \sim Q_2^2$ on flow maps since $Q_{\text{T}} \sim Q_2$ for $\varphi \ll 1$ in the engulfment regime. The fragmentation of small miscible threads is interpreted as resulting from the coupling between inertial disturbances causing local variations in thread diameter and diffusion blending thin thread edges. Furthermore, viscous threads can also experience diffusion-induced buckling instabilities as shown with transition line (iii) in the subregime diffusive buckling. In this case, progressively diverging threads experience compact coiling deformation during diffusive swelling [12].

To better delineate diffusive flows, we systematically explore very low flow velocities with fine variations of flow rates for fluid pair C3-2, i.e., for isopropanol. Two main diffusive regimes are observed, including an “ultradiffusive” regime, where the thread diameter is found to significantly swell due to molecular diffusion in the outlet channel at low Q_1 , and a “winged” regime that corresponds to a diffusive bulging where the fluid $L1$ diffuses in the upstream channels of $L2$ at low Q_2 . In the case of partially miscible fluids between our silicone oil and polar organic solvents, intriguing discrete structures are observed in the upstream channels at large Q_1 due to fluid saturation while continuous diffusive pools are observed at low Q_1 . Hence, the winged regime is divided in two subregimes with a transition line found at constant Q_1 as indicated with line (iv) in Fig. 3. Next, we examine in detail the diffusive and winged regimes and investigate the evolution of the thread detachment length. We show that the diffusive boundaries of the flow map are better understood by examination of individual flow characteristics.

B. Thread diameter

We first examine the evolution of the normalized thread diameter ε_0/h in the base flow regimes. Solving Stokes equations for a core-annular configuration in a circular duct of diameter h yields a simple relation between core diameter ε_0 , flow rate ratio φ , and viscosity contrast χ , such as

$$\frac{\varepsilon_0}{h} = \sqrt{\frac{1 + \varphi - \sqrt{1 + \varphi\chi^{-1}}}{2 + \varphi - \chi^{-1}}}. \quad (1)$$

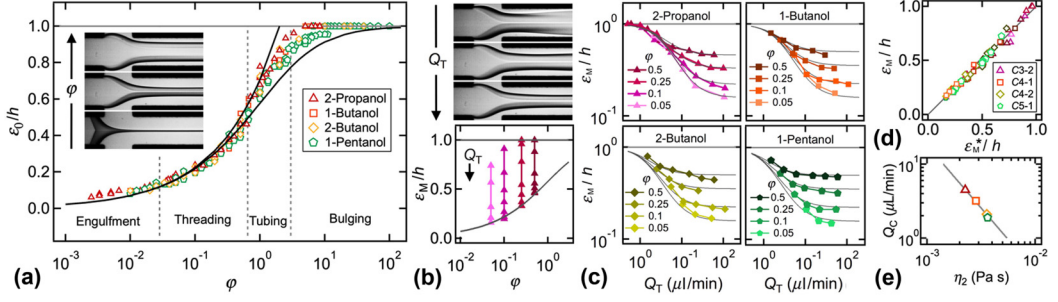


FIG. 4. Diameter of miscible fluid threads. (a) Evolution of stable diameter ε_0/h as a function of flow rate ratio φ across structural flow regimes. Lower solid line: Eq. (2), upper solid line: Eq. (3). (b) Variation of minimum diameter ε_M/h as a function of φ showing the role of Q_T on iso- φ curves for fluid pair C3-2. (c) Evolution of ε_M/h with Q_T along iso- φ curves for miscible fluid pairs, fitting parameter $Q_C = 4.5$ (2-propanol), 3.2 (1-butanol), 2.1 (2-butanol), and 1.6 $\mu\text{l}/\text{min}$ (1-pentanol). (d) Comparison of measured ε_M/h with Eq. (4). (e) Evolution of Q_C with solvent viscosity η_2 .

The case of large viscosity contrasts, $\chi \gg 1$, corresponds to an asymptotic regime where the normalized thread diameter ε_0/h only depends on flow rate ratio φ and is approximated according to

$$\frac{\varepsilon_0}{h} = \left(\frac{\varphi}{2 + \varphi} \right)^{1/2}. \quad (2)$$

This expression can be further simplified for low flow rate ratio $\varphi \ll 1$, with the scaling

$$\frac{\varepsilon_0}{h} = \left(\frac{\varphi}{2} \right)^{1/2}. \quad (3)$$

While scaling analysis is useful to study the behavior of small threads, Eq. (2) represents a bounded function and provides a practical approximation of the confined nature of microfluidic threads having a size ε_0/h that tends to unity for very large φ . Here, we measure the size of miscible fluid threads as a function of φ in the nondiffusive primary regimes, including engulfment, threading, tubing, and bulging, and find good agreement with Eq. (2), which represents the lower bounding curve on Fig. 4(a), while the upper bounding curve is set with scaling defined in Eq. (3). Thread sizes in the tubing regime are expected to deviate from the analytical solution of a circular tube since this case corresponds to a partial thread lubrication, with a thread contact with top and bottom walls and a stratified flow near the side walls. As a result, thread size appears to follow Eq. (3) in the tubing regime before saturating at $\varepsilon_0/h = 1$ in the bulging regime for $\varphi > 3$. Over the range of parameters investigated, however, Eq. (2) provides a more realistic estimate of basic confined thread sizes at large Q_T and can be used as a reference in the study of diffusive effects at low Q_T . The fact that ε_0/h solely depends on φ at large viscosity contrast $\chi \gg 1$ hints at the development of a method that consists in examining the evolution of thread size at fixed φ and various Q_T . An example of this approach is shown in Fig. 4(b), top, where the minimal thread size ε_M/h observed in the central channel near the junction is seen to decrease with Q_T for $\varphi = 0.5$. Generalizing this technique to various φ shows that the minimum value of the diffusive thread size ε_M along an iso- φ curve tends to the stable thread size ε_0 at large Q_T [Fig. 4(b), top]. By contrast, the normalized diffusive thread size ε_M/h tends to unity at low Q_T . Considering the boundary conditions of ε_M/h , we recently discuss [12] the use of simple bounded functions, which—similarly to Eq. (2) with ε_0/h and φ —provide a good approximation of the evolution of ε_M/h as a function of Q_T according to

$$\frac{\varepsilon_M^*}{h} = 1 - \frac{1}{\frac{1}{1 - \varepsilon_0/h} + \left(\frac{Q_T}{Q_C} \right)^{-1.5}}. \quad (4)$$

The exponent -1.5 corresponds to the steepness of iso- φ curves and is considered as a phenomenological constant for all fluid pairs. By contrast, the critical flow rate Q_C depends on each fluid pair and is determined experimentally as the sole fitting coefficient of the iso- φ curves of ε_M/h as a function of Q_T as shown in Fig. 4(c). To verify the accuracy of the method of determining Q_C , all measured ε_M/h are plotted against Eq. (4) with their corresponding Q_C in Fig. 4(d). Overall, examining diffusive swelling of threads enables the fine determination of Q_C , which permits an estimation of diffusion coefficient D_{12} based on similitude analysis [12] with a critical Péclet number,

$$\text{Pe}_C = Q_C/(D_{12}h) = 850. \quad (5)$$

Here, we find that Q_C decreases with the viscosity of the alcohol phase as shown in Fig. 4(e). The experimental identification of a critical flow rate Q_C associated with each fluid pair is advantageous in characterizing the role of diffusion on thread swelling across fluid pairs. Indeed, Eq. (5) shows that the kinematic quantity Q_C , which is the sole fitting parameter in Eq. (4), depends on fluid properties and geometry according to $Q_C = \text{Pe}_C D_{12} h$ and the Péclet number scales as $\text{Pe} \sim Q_T/Q_C$, a formulation reminiscent of the capillary number $\text{Ca} \sim V/V^*$, where the characteristic velocity $V^* = \gamma_{12}/\eta$. Therefore, a similar approach, which consists in determining a characteristic flow rate, is employed to discuss other aspects of diffusive fluid threads, including the detachment length and the winged regime.

C. Detachment length

A remarkable property of liquid-liquid flows resides in the possibility to sheath viscous material in a low-viscosity continuous phase using hydrodynamic focusing junctions. As the thick fluid is injected from the central channel, the thin liquid injected from the side channels progressively encapsulates the thread, which detaches from the top and bottom walls along oblique, apparent miscible contact lines [Fig. 5(a)]. Contact lines typically adopt the shape of slanted straight lines initially drawn from the side walls at x_0 and joining in the center of the channel further downstream at x_1 to form the shape of a triangle, as indicated in the schematics in the inset of Fig. 5(b). As the flow rate ratio φ increases, separation lines move downstream and the triangle longitudinally deforms and forms curved contact lines. In previous work [41], the distance from the channel junction at $x = 0$ to the contact point of miscible contact lines, i.e., the position of the separation point located at coordinate x_1 , is referred to as the formation length L_S . In the threading regime, L_S follows a scaling of the form $L_S/h \sim \chi\varphi$ at large χ and remains independent of viscosity with $L_S/h \sim \varphi$ below a moderate ratio $\chi < 10^2$. This quantity is important to define the transition to the engulfment regime, which corresponds to $L_S/h \sim 0$ for low $\varphi \sim \varphi_{\text{Eng}}$. Comparatively, the transition to the tubing regime is defined when $L_S/h \gg 1$ for large $\varphi > \varphi_{\text{Tub}}$. Detailed examination of engulfment and threading regimes, however, reveals the smooth evolution of the width, $x_1 - x_0$, of the contact line triangle over a wide range of flow rate ratios φ [Fig. 5(a)]. Hence, we generalize and extend the criterion for predicting high-viscosity fluid encapsulation in square focusing sections and measure the intrinsic thread detachment length as $L_D = x_1 - x_0$ as a function φ across base flow regimes, i.e., engulfment, threading, and tubing regimes. As can be seen in Fig. 5(b), measurements of L_D in the viscous regimes yield a robust scaling, which is referred to as the stable detachment length L_{D0} according to

$$\frac{L_{D0}}{h} = 1.9\varphi^{1/2}, \quad (6)$$

for miscible fluid pairs at large Q_T . Incidentally, while entry length scales are typically measured starting from the fluid junction at $x/h = 0$, the occurrence of the engulfment regime with the intrusion of the outer fluid $L2$ in the upstream central channel challenges the definition of a physical length scale based on the evolution of a single coordinate, such as $L_S = x_1$. An example of the evolution of coordinates x_0 and x_1 is shown in Fig. 5(c) where regime transitions are closely related

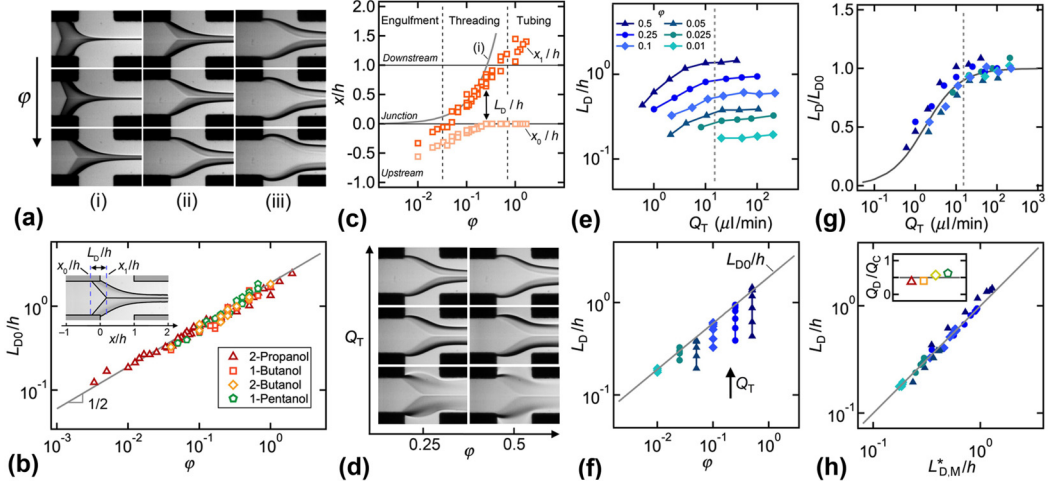


FIG. 5. Viscous detachment length L_D of miscible fluid threads. (a) Micrographs of fluid contactor in primary flow regimes, fluid pair C3-2, from top to bottom: (i) $\varphi = 2.5 \times 10^{-3}$, 1×10^{-2} , 2.5×10^{-2} , (ii) $\varphi = 5 \times 10^{-2}$, 1×10^{-1} , 2.5×10^{-1} , and (iii) $\varphi = 3.3 \times 10^{-1}$, 5×10^{-1} , 1×10^0 . (b) Evolution of stable detachment length L_{D0}/h as a function of φ . Solid line: Eq. (6). Inset: schematics of measurement of L_D . (c) Variation of initial and final viscous detachment locations, x_0 and x_1 , as a function of φ for fluid pair C4-1. Solid line (i): $x/h = 3.84\varphi$. (d) Chart of micrographs showing a reduction of L_D for diffusive regimes at low Q_T . (e) Evolution of L_D/h as a function of Q_T along iso- φ curves for fluid pair C3-2. (f) Evolution of L_D/h as a function of φ along iso- φ curves for fluid pair C3-2. Solid line: Eq. (6). (g) Evolution of L_D/L_{D0} as a function of Q_T with fluid pair C3-2. Solid line: $L_D/L_{D0} = (1 + Q_D/Q_T)^{-1}$ with $Q_D = 1.7 \mu\text{l/min}$. (h) Comparison of L_D/h and $L_{D,M}^*/h$ calculated based on Eq. (7). Inset: evolution of Q_D/Q_C for miscible fluid pairs. Solid line: $Q_D/Q_C = 0.5$.

to the values of x_1 . A subtransition in the threading regime can be defined when $x_0 = 0$, which occurs for $\varphi_{\text{Thread}} \sim 5 \times 10^{-1}$. For flow rates below φ_{Thread} , the partial engulfment of L2 is observed as $x_0 < 0$, while above φ_{Thread} , viscous ensheathing entirely takes place at the junction.

The stable detachment length L_{D0}/h of base regimes at large Q_T provides a useful reference in the study of diffusive flows at low Q_T . In the diffusive regime, we examine the evolution of the detachment length L_D along iso- φ curves and L_D is found to initially grow with flow rate Q_T before flattening toward L_{D0} at larger flow velocity in the viscous regime. Examples of diffusive thread-forming flow morphologies at various Q_T are shown in Fig. 5(d) for two cases with fixed φ . In Figs. 5(d) and 5(f), we use the iso- φ approach to characterize the evolution of L_D based on absolute and relative flow rates, Q_T and φ , for fluid pair C3-2. The asymptotic behavior of L_D at large Q_T indicates the bounded nature of the function L_D/L_{D0} , which tends to 0 at low Q_T and 1 at large Q_T . Hence, the scaled detachment length is modeled with a simple bounded function $L_D/L_{D0} = (1 + Q_D/Q_T)^{-1}$, which shows good agreement with data when the characteristic flow rate is set at $Q_D = 1.7 \mu\text{l/min}$ for fluid pair C3-2 [Fig. 5(g)]. Overall, our data support the definition of the function

$$\frac{L_{D,M}^*}{h} = 1.9 \frac{\varphi^{1/2}}{1 + (Q_T/Q_D)^{-1}} \quad (7)$$

to model the viscous detachment length L_D with miscible fluid pairs [Fig. 5(b)]. The characteristic flow rate Q_D is measured for each miscible fluid pair and the nearly constant ratio $Q_D/Q_C \sim 0.5$ [Fig. 5(h), inset] suggests proportionality between Q_D and intermolecular diffusion coefficient D_{12} . Hence, the term Q_T/Q_D is expected to be proportional to the Péclet number Pe . In the

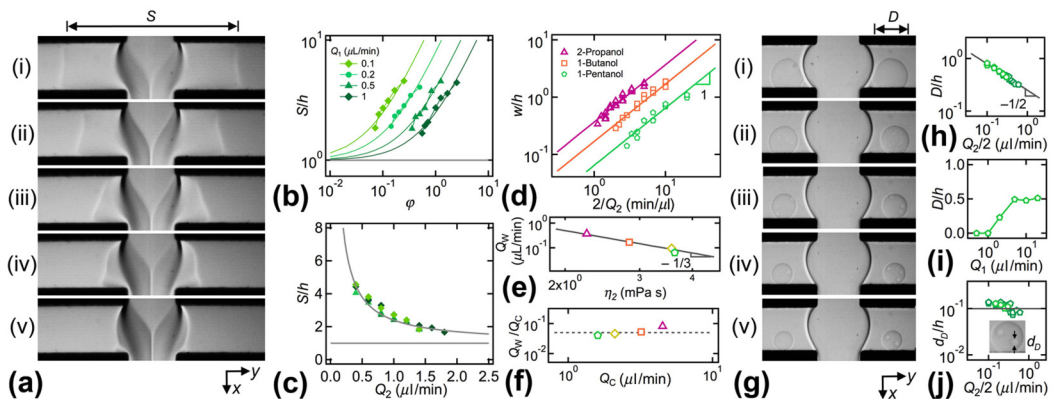


FIG. 6. Winged thread regime. (a) Micrographs showing lateral span S of diffusive pools for fluid pair C3-2, flow rates in $\mu\text{l}/\text{min}$, $Q_1 = 0.5$ and $Q_2 =$ (i) 0.5, (ii) 0.7, (iii) 0.9, (iv) 1.1, and (v) 1.3. (b) Evolution of normalized span S/h as a function of φ for various iso- Q_1 curves for fluid pair C3-2. Solid lines: $S/h = 1 + 1.5\varphi/Q_1$. (c) Span S/h versus Q_2 for data corresponding to (b). Solid line: $S/h = 1 + 1.5/Q_2$. (d) Variation of normalized pool width w/h versus reciprocal flow rate $2/Q_2$ for $Q_1 \leq 1 \mu\text{l}/\text{min}$. Solid lines: $w/h = 2Q_W/Q_2$. (e) Evolution of Q_W with solvent viscosity η_2 ; solid line: $Q_W = 4\eta_2^{-1/3}$. (f) Ratio Q_W/Q_C ; solid line: $Q_W/Q_C = 5 \times 10^{-2}$. (g) Micrographs showing saturated circulating regions with fluid pair C5-1 at large $Q_1 = 5$ and $Q_2 =$ (i) 0.2, (ii) 0.3, (iii) 0.4, (iv) 0.5, and (v) 0.6. (h) Evolution of normalized island size D/h versus $Q_2/2$ for $Q_1 \geq 2 \mu\text{l}/\text{min}$. Solid line: $D/h = 2.5 \times 10^{-1}(Q_2/2)^{-1/2}$. (i) Evolution of D/h with Q_1 for fixed $Q_2 = 0.5$. (j) Measurement of normalized subdroplet size d_D/h with $Q_2/2$. Solid line: $d_D/h = 0.1$.

context of facilitating direct comparison between miscible and immiscible fluid pairs, however, we elect mathematical formulations based on relative and absolute flow rates, φ and Q_T , instead of dimensionless numbers such as Pe and Ca.

D. Winged thread regime

We now turn our attention to an intriguing flow pattern of miscible fluid threads, which occurs at very low flow rates and is referred to as a “winged thread” regime. This regime is characterized by the appearance of diffusion layers extending upstream of the focusing section in the side channels of fluid L_2 . Hence, in the focusing section, the thread develops lateral diffusive pools, which vaguely resemble wings that are used as a reference to label this highly diffusive flow structure. This pattern is distinct from the bulging regime, which occurs at large $\varphi > 3$ and where lateral protrusions are made of pure liquid L_1 . By contrast, the winged regime is also found at low φ and protrusions are made of a mixture of L_1 and L_2 as can be seen in Fig. 6(a). Diffusive pools of variable indices of refraction appear to extend on either side of the thread over a span S , which is measured for fixed Q_1 as a function of φ on Fig. 6(b) and as a function of Q_2 in Fig. 6(c) for fluid pair C3-2. Experimental measurements of S/h are well fit with an expression of the form $S/h = 1 + Q_{WS}/Q_2$ where the constant $Q_{WS} = 1.5 \mu\text{l}/\text{min}$ is associated with fluid pair C3-2. The presence of diffusive pools evolving at counterflow of the side fluid L_2 offers the opportunity to probe the influence of fluid properties on flow morphology. To simplify the analysis, we focus on scaling behaviors and investigate the evolution of the lateral extent of a single diffusive pool $w = (S-h)/2$ in a single channel as a function of incoming side channel flow rate $Q_2/2$ for various fluid pairs [Fig. 6(d)]. Over the range of parameters investigated with $Q_1 \leq 1 \mu\text{l}/\text{min}$, we find a relation of the form $w/h = 2Q_W/Q_2$ where the constant $Q_W = 4Q_{WS}$ decreases with side fluid viscosity η_2 [Fig. 6(e)] and linearly scales with the critical flow rate of diffusive threads Q_C , such as $Q_W/Q_C \approx 5 \times 10^{-2}$ [Fig. 6(f)]. Therefore, using Eq. (5), the width of a diffusive wing in the focusing section can be

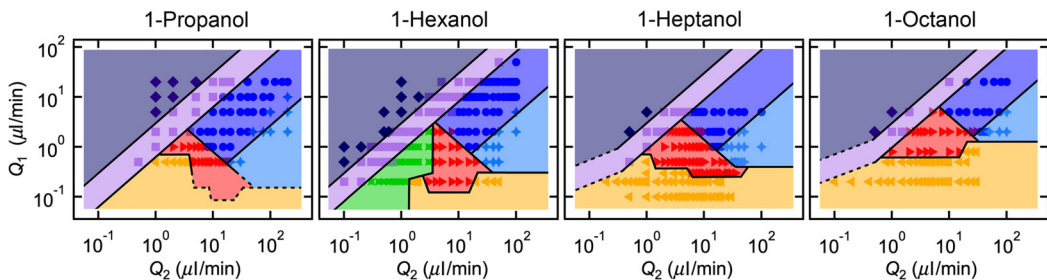


FIG. 7. Flow maps of immiscible fluid pairs, C3-1 (1-propanol), C6-1 (1-hexanol), C7-1 (1-heptanol), and C8-1 (1-octanol), including threading (●), tubing (■), engulfment (◆), bulging (◆), jetting (▶), dripping (◀), and wetting (×) regimes. Dashed lines represent regime extrapolations drawn from analogy between maps. See main text for solid transition lines.

estimated according to $w/h \sim 85/Pe_2$, where the Péclet number $Pe_2 = Q_2/(D_{12}h)$ is associated with incoming flow of a single side square microchannel.

Another region of the winged thread regime is found at larger central stream flow rate $Q_1 \geq 2 \mu\text{l}/\text{min}$, where discrete structures typically appear instead of continuous pools [Fig. 6(g)]. The formation of such structures results from the complex interplay between the enhanced flux of $L1$ through the section as well as potentially from the saturation concentration of partially miscible fluid pairs made of oils and polar organic solvents. In the case of pentanol with fluid pair C5-1, we measure the size D of such circular “islands,” which remain constant over time, and find a simple correlation $D/h \sim (Q_2/2)^{-1/2}$ [Fig. 6(h)]. Our data also suggest that D remains relatively independent of Q_1 at large flow rates [Fig. 6(i)]. Detailed examination of the internal structure of these islands also reveals the presence of embedded droplets of very small size $d_D/h \sim 10^{-1}$ [Fig. 6(j)], indicating complex coupling between physicochemical and hydrodynamic processes. Indeed, islands appear located in the low-pressure region of the hydrodynamic focusing section and are observed to undergo stationary rotation.

V. CAPILLARY THREADS

A. Flow maps

We now examine the flow maps of immiscible fluid threads (Fig. 7). Similar to their miscible fluid counterparts, base flow regimes of capillary threads are found at relatively large flow rates Q_T , in the upper right region of the flow maps while droplet regimes are located in the lower part of the diagrams. The overall form of flow maps of immiscible fluid pairs with $\chi \gg 1$ in orthogonal focusing sections with square microchannels is similar to previous work [42] conducted at larger interfacial tension γ_{12} . Here, we merge notation between “displacement” and “bulging” regimes, which are found at large $\varphi > 3$ from moderate Q_T . Critical curves for the tubing-threading and the threading-engulfment regime transitions for each fluid pair show good agreement with previous correlations of base flow regimes [41] and are defined with oblique lines of fixed φ , which solely depend on χ . At low flow rates Q_T , interfacial properties considerably alter flow regimes with the presence of dispersed flows and a shift toward larger φ is observed for bulging and tubing transition at higher values of γ_{12} with fluid pairs C7-1 and C8-1. The most significant outcome of interfacial tension consists in the formation of droplet flow regimes, namely, the dripping regime, where droplets are formed at the fluid junction, and the jetting regime, where droplets are emitted from the tip of the capillary threads. Over the range of fluids investigated, we also found a strong influence of wetting properties at low flow rates due to the partial wetting condition of silicone oil–alcohol fluid pair on borosilicate glass. We find that wetting properties can modify droplet formation in the dripping regime and central thread encapsulation in the jetting regime. Indeed,

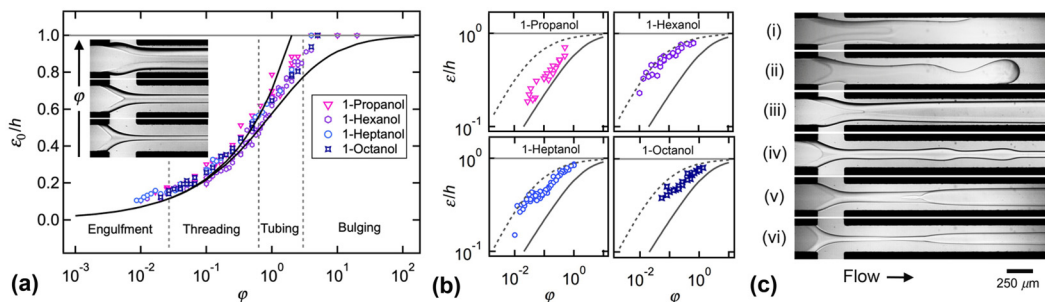


FIG. 8. Diameter of immiscible fluid threads. (a) Evolution of stable diameter ε_0/h as a function of flow rate ratio ϕ in the viscous regime. Lower solid line: Eq. (2); upper solid line: Eq. (3). Inset: micrographs of stable regimes with fluid pair C8-1. (b) Evolution of width ε/h in the capillary regime with partial lubrication due to thread wetting. Solid line: Eq. (2); dashed line: Eq. (8). (c) Micrographs of wetting threads, flow rates (Q_1, Q_2) in $\mu\text{l}/\text{min}$, (i) fluid pair C6-1 (0.2, 0.2), (ii) (0.2, 0.8), (iii) fluid pair C7-1 (2, 2), fluid pair C8-1 (0.8, 15), (v) fluid pair C6-1 (2,10), and (vi) (0.5, 30).

a thread can experience an asymmetrical detachment from top and bottom walls due to wetting in the jetting regime. However, the presence of strong capillary waves developing along the core is a clear indication of jetting flows and, as a result, such flow patterns are reported as jetting flows. In the case of dripping flows, strong dynamic wetting can suppress the formation of droplets at low Q_T , which is significant with fluid pair C6-1 (Fig. 7). The overall transition from dispersed to separated flows is shifted toward larger flow rates as γ_{12} increases from fluid pairs C3-1 to C8-1. For instance, the dripping-threading transition is found at larger Q_1 and the jetting-threading transition, defined as a fixed value of the product $Q_1 Q_2$, is also shifted toward higher values for larger values of γ_{12} from 1-propanol to 1-octanol. In the following, we discuss complementary aspects of immiscible fluid flows.

B. Thread diameter

In this section, we analyze the evolution of normalized thread diameter ε/h with immiscible fluid pairs (Fig. 8). Stable thread diameters ε_0/h are measured in the base flow regimes, including engulfment, threading, tubing, and bulging, and show good agreement with Eqs. (2) and (3) in a fashion similar to the miscible fluid cases in the viscous regime at relatively large Q_T [Fig. 8(a)]. In the capillary regime at lower Q_T , however, viscous threads display a variety of morphologies due to incomplete lubrication and dynamic wetting. Indeed, the relatively low value of advancing contact angles in partial dynamic wetting conditions at low velocities favors thread adhesion to microchannel walls and as a result the central stream adopts intermediate behavior between core-annular flows and viscous stratifications. Measurements of central width ε/h as a function of ϕ in the presence of partial wetting conditions show data bounded between a lower curve defined by stable diameter ε_0/h of core-annular flows based on Eq. (2) and the width ε_S/h of viscous stratifications [Fig. 8(b)]. The strata width ε_S/h is estimated based on previous work [50] with fluids having low $\chi < 1$ in square microchannels using a relation of the form

$$\frac{\varepsilon_S}{h} = \frac{1}{1 + 0.67\phi^{-2/3}\chi^{-1/2}}. \quad (8)$$

Here, this relationship is extrapolated to the case of large $\chi \gg 1$ that would otherwise form lubricated viscous threads through viscous self-lubrication in the absence of wetting phenomena. In general, loss of lubrication results in stream deceleration due to significant shear at the microchannel walls, which is accompanied with a stream width enlargement to conserve mass. Hence, while ε_0/h of threads does not depend on χ , the strata width ε_S is contingent on χ as shown in Eq. (8).

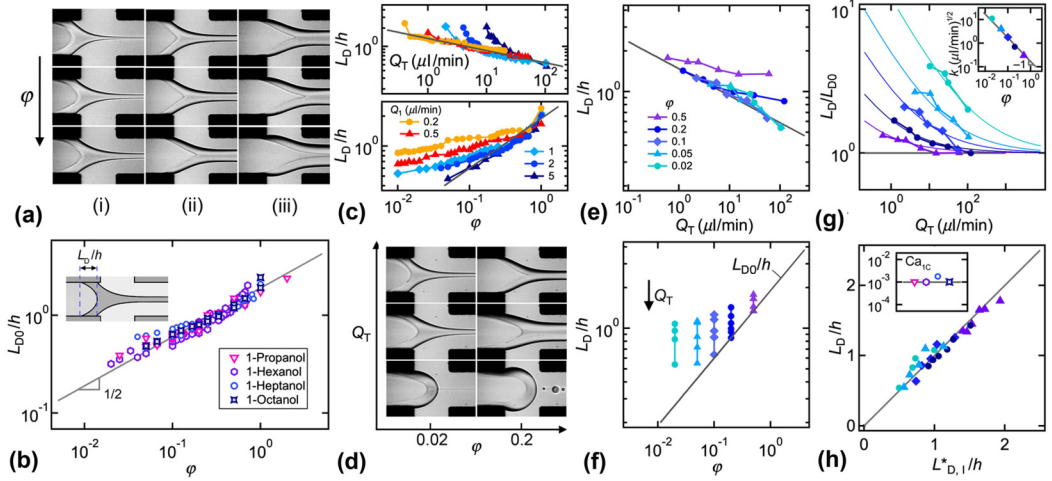


FIG. 9. Detachment length L_D of immiscible fluid threads. (a) Micrographs of fluid contactor in primary flow regimes, fluid pair C7-1, from top to bottom: (i) $\varphi = 1 \times 10^{-2}, 2 \times 10^{-2}, 2.5 \times 10^{-2}$; (ii) $\varphi = 5 \times 10^{-2}, 1 \times 10^{-1}, 2.5 \times 10^{-1}$; and (iii) $\varphi = 3.3 \times 10^{-1}, 5 \times 10^{-1}, 1 \times 10^0$. (b) Evolution of stable detachment length L_{D0}/h as a function of φ in the viscous regime. Solid line: Eq. (6). (c) Evolution of L_D/h as a function of Q_T and φ along iso- Q_1 curves, fluid pair C7-1. Solid lines: $L_D/h = 0.87Q_T^{-0.2}$ (top) and $L_D/h = 1.9\varphi^{1/2}$ (bottom). (d) Chart of micrographs showing an increase of L_D for capillary regimes at low Q_T . Fluid pair C8-1, flow rates (Q_1, Q_2) in $\mu\text{l}/\text{min}$, from top to bottom, $\varphi = 0.02$ (2, 100), (0.8, 30), (0.2, 10), and $\varphi = 0.2$ (20, 100), (0.8, 4), and (0.2, 1). (e) Evolution of L_D/h as a function of Q_T along iso- φ curves for fluid pair C8-1. Solid line: $L_D/h = Q_T^{-0.2}$. (f) Evolution of L_D/h as a function of φ along iso- φ curves for fluid pair C8-1. Solid line: Eq. (6). (g) Scaled length L_D/L_{D0} versus Q_T . Solid lines: $L_D/L_{D0} = 1 + kQ_T^{-1/2}$. Inset: coefficient k as a function of φ . Solid line $k = k_0\varphi^{-1}$ with $k_0 = 0.17(\mu\text{l}/\text{min})^{1/2}$. (h) Comparison of L_D/h with Eq. (9).

Examples of characteristic wetting behavior are displayed in Fig. 8(c), including the wetting-induced suppression of dripping regimes at low Q_2 with 1-hexanol, partial separation and reattachment of contact line, the formation of bead-on-thread during jetting, and lubrication failure of small threads.

C. Detachment length

In this section, we examine the detachment length of capillary threads. Similar to their diffusive counterparts, viscous threads formed between immiscible fluids progressively detach from top and bottom walls at the fluid junction. At relatively large Q_T , contact lines adopt a triangular shape, characteristic of the viscous regime [Fig. 9(a)]. By contrast, the contact lines are more curved at low Q_T in the capillary regime. The stable detachment length L_{D0}/h of immiscible threads is measured as a function of φ in the viscous regime and good agreement is found with Eq. (6) of miscible threads as can be seen in Fig. 9(b). The behavior of L_D/h at low Q_T , however, significantly differs from that in the viscous regime and observed lengths are found in excess of L_{D0}/h . In Fig. 9(c), we examine the evolution of L_D/h along iso- Q_1 curves for fluid pair C7-1, which shows a rather complex, yet regular, dependency of L_D/h on both absolute and relative flow rates, Q_T and φ . While examining iso- Q_1 curves is useful since in practice it is convenient to fix the high-viscosity fluid flow rate Q_1 and vary the low-viscosity fluid flow rate Q_2 to collect data, the evolution of iso- Q_1 curves is difficult to interpret. Therefore, we rationalize the evolution of L_D/h based on parameters such as φ and Q_T and show that for a fixed flow rate ratio φ , the detachment length of immiscible threads decreases with Q_T , which is in the opposite trend of miscible threads [Fig. 9(d)]. In the dripping regime, L_D/h periodically varies during the droplet emission process with an increase during droplet

squeezing and a decrease after droplet detachment. Therefore, we measure the minimal length after detachment as the reference data of L_D/h and find that this quantity remains significantly larger than L_{D0}/h . To develop an empirical relationship for L_D/h , we first compare the evolution of L_D/h along iso- φ curves as a function of Q_T and φ in Figs. 9(f) and 9(e). Since L_D/h tends to L_{D0}/h at large Q_T , we plot the evolution of L_D/L_{D0} as a function of Q_T in Fig. 9(g) and observe the ungrouping iso- φ curves at low Q_T and their convergence toward unity at large Q_T . Overall, curves are well fitted using the simple analytical function $L_D/L_{D0} = 1 + kQ_T^{-1/2}$ where the coefficient k is found to depend on φ according to $k = k_0\varphi^{-1}$ [Fig. 9(g), inset]. Since the coefficient k_0 depends on the specific fluid pair, we find it useful to express this quantity in the form of a critical flow rate, such as $k_0 = Q_D^{1/2}$, which enables the definition of the function

$$\frac{L_{D,1}^*}{h} = 1.9\varphi^{1/2}[1 + \varphi^{-1}(Q_T/Q_D)^{-1/2}], \quad (9)$$

which is in good agreement with experimental data [Fig. 9(h)]. Next, we relate the characteristic Q_D with fluid properties and flow geometry and calculate the critical capillary number $Ca_{1C} = \eta_1 Q_D / (\gamma_{12} h^2)$, which remains nearly constant, $Ca_{1C} \sim 10^{-3}$, for the immiscible fluid pairs [Fig. 9(h), inset]. Hence, the term Q_T/Q_D is expected to be proportional to the capillary number Ca/Ca_{1C} . Comparing Eq. (7) of diffusive threads to Eq. (9) of capillary threads underscores major differences between miscible and immiscible thread behavior in microfluidic flow contactors, where L_D increases with Q_T for diffusive flows and L_D decreases with Q_T for capillary flows. In both cases, however, a similar viscous regime is recovered at larger Q_T due to the predominance of the role of viscosity in confined microsystems.

D. Droplet regimes

Finally, we investigate the dynamics of droplet regimes through analysis of periodic flow patterns of dripping and jetting droplets. Parameters of interest include droplet size d and spacing L , as well as velocity V and frequency f of emission. The droplet size d consists in the longitudinal length of confined droplets as this parameter controls the overall morphology of segmented flows. In the dripping regime, previous work [42] showed that for relatively large values of γ_{12} at $\chi \gg 1$, measurements of normalized droplet size d/h depend on parameter $\alpha_2 Ca_2$, where the side flow liquid fraction $\alpha_2 = Q_2 / (Q_1 + Q_2)$ and the side flow capillary number $Ca_2 = \eta_2 Q_2 / (\gamma_{12} h^2)$. Here, data show good agreement with previous scaling where $d/h \sim (\alpha_2 Ca_2)^{-1}$ for large droplets and $d/h \sim (\alpha_2 Ca_2)^{-0.17}$ for smaller droplets [Fig. 10(a)]. Given the very low values of γ_{12} examined in the current study, however, most droplets display small d and form in the diluted regime at low φ , which corresponds to modest variation of α_2 between 0.5 and 1. As a result, data points also collapse onto a single curve as a function of Ca_2 , which is well fitted with a simplified scaling of the form $d/h = 0.3Ca_2^{-1/3}$ [Fig. 10(a), inset]. By similitude with the behavior of fluid pairs C6-1, C7-1, and C8-1, where interfacial tension γ_{12} is determined using a tensiometer, the value of $\gamma_{12} = 0.1$ mN/m for fluid pair C3-1 is deduced in agreement with scaling relationships of dripping droplets. Experimental micrographs of a dripping droplet with evolution of both d and L are shown in Fig. 10(b).

In the jetting regime, the droplet size is proportional to the thread diameter ε and can be estimated using the scaling $d/h = 3.1\varphi^{1/2}$ for χ varying between 12 and 47, as seen in Fig. 10(c). Overall, the jetting regime displays a variety of flow morphologies as capillary waves propagate along the viscous thread before rupturing into droplets. Near the threading transition, viscous tails leading to satellite droplets are typically observed during breakup. In the case of very long tails, small filaments can also break through jetting as seen in Figs. 10(b)(v) and 10(d)(v). As regularly emitted droplets form steady periodic patterns, the droplet velocity quickly reaches its terminal velocity V_D , which depends on both size d and total capillary number $Ca_T = Q_T \eta_2 / (h^2 \gamma_{12})$ [Fig. 10(e)]. Overall, the droplet velocity V_D can be reasonably approximated with the total superficial velocity $J_T = Q_T/h^2$ [Fig. 10(e), inset]. The aspect ratio of segmented flow is characterized by the droplet

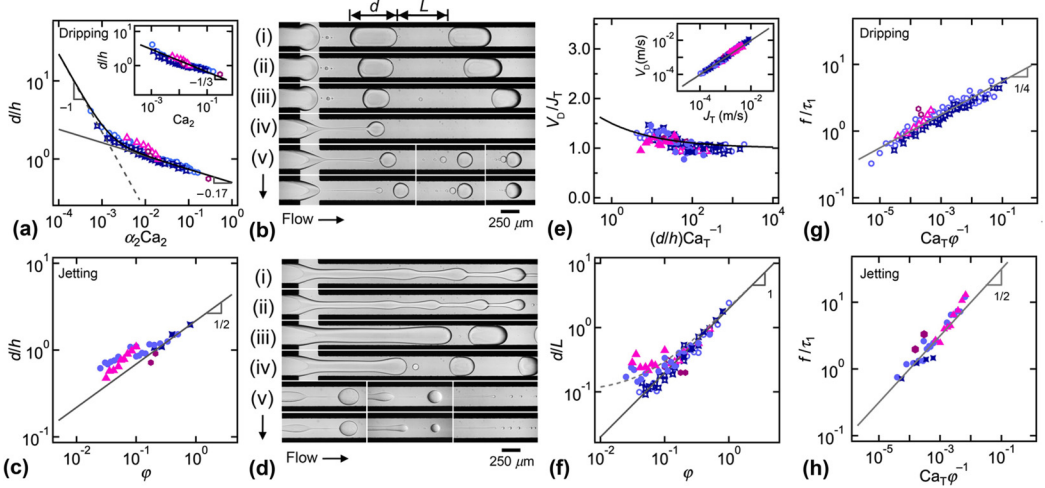


FIG. 10. Droplet regimes with dripping (open symbols) and jetting (solid symbols) patterns. (a) Evolution of normalized dripping droplet size d/h as a function of $\alpha_2 Ca_2$. Dashed line: $d/h = 2.2 \times 10^{-3} (\alpha_2 Ca_2)^{-1}$, solid line: $d/h = 0.5 (\alpha_2 Ca_2)^{-0.17}$. Inset: droplet size d/h versus capillary number Ca_2 , solid line: $d/h = 0.3 Ca_2^{-1/3}$. (b) Micrographs of dripping droplets, flow rates in $\mu\text{l}/\text{min}$, fluid pair C8-1, $Q_1 = 0.1$, $Q_2 =$ (i) 0.2, (ii) 0.6, (iii) 1, (iv) 10, and (v) time series of dripping tail breakup with $Q_1 = 0.5$ and $Q_2 = 10$. (c) Jetting droplet size with flow rate ratio ϕ , solid line: $d/h = 3.1 \phi^{1/2}$. (d) Micrographs of jetting droplets with flow rates (Q_1, Q_2); (i) fluid pair C-71 (0.5, 6); (ii) (0.3, 9); (iii) fluid pair C-81 (0.8, 1); (iv) (0.5, 2); (v) fluid pair C-31 (0.5, 5), (0.5, 7), (0.5, 10), (0.5, 16); and fluid pair C8-1 (0.3, 30) and (0.3, 35). (e) Evolution of normalized droplet velocity V_D/J_T as a function of $(d/h)Ca_T^{-1}$. Solid line: $V_D/J_T = 1 + 0.5[d/(hCa_T)]^{-1/3}$. Inset: droplet velocity V_D as a function of J_T ; solid line: $V_D = J_T$. (f) Evolution of segmented flow aspect ratio d/L with flow rate ratio ϕ . Solid line for dripping: $d/L = 2\phi$. Dashed line for jetting: $d/L = 0.1 + 2\phi$. (g) Normalized emission frequency of dripping droplet f/τ_1 as a function of $Ca_T \phi^{-1}$. Solid line: $f/\tau_1 = 10(Ca_T \phi^{-1})^{1/4}$. (h) Normalized emission frequency of jetting droplet f/τ_1 as a function of $Ca_T \phi^{-1}$. Solid line: $f/\tau_1 = 10^2(Ca_T \phi^{-1})^{1/2}$.

size to spacing, d/L , which remains essentially proportional to the flow rate ratio ϕ since for a unit cell $\lambda = d + L$ emitted during time period T , the intrinsic mass conservation argument indicates that $d \sim Q_1 T/h^2$ and $L \sim Q_2 T/h^2$ [Fig. 10(f)]. The period of droplet emission T can be estimated based on frequency as $T = 1/f$ and together with the basic wave equation $f = V/\lambda$, one would expect $f \sim J_T/(d + L)$. Here, we develop a simple scaling for the frequency based on external control parameters and normalize the frequency f with the viscous fluid injection shear rate $\tau_1 = Q_1/h^3$ since in the diluted dripping regime with $d \sim h$, one would expect $f \sim \tau_1$. The normalized frequency is shown to weakly depend on parameter $Ca_T \phi^{-1}$ with $f/\tau_1 \sim (Ca_T \phi^{-1})^{1/4}$ for a dripping droplet [Fig. 10(g)] and $f/\tau_1 \sim (Ca_T \phi^{-1})^{1/2}$ for jetting droplets [Fig. 10(h)]. The parameter $Ca_T \phi^{-1}$ is found to collapse all data points for all immiscible fluid pairs investigated.

VI. CONCLUSIONS

This study provides a comprehensive examination of the role of fluid properties during the formation of viscous fluid threads in microchannels. A series of a low molecular weight primary and secondary alcohols is used together with a single oil to initiate capillary thread destabilizations when fluids are immiscible and diffusive thread swelling when fluids are miscible. In the viscous regime at relatively large flow rates, both diffusive and capillary threads display similar behavior in terms of thread diameter $\varepsilon_0/h \sim 0.7\phi^{1/2}$ and detachment length $L_{D0}/h \sim 1.9\phi^{1/2}$, which yields a nearly constant aspect ratio $L_{D0}/\varepsilon_0 \sim 2.7$. At lower flow rates, however, our comparative study reveals different thread behaviors depending on fluid molecular affinity. For miscible fluid pairs, the thread

diameter ε_M is shown to swell in the diffusive regime and decreases with Q_T toward ε_0 . By contrast, the detachment length L_D grows with Q_T and tends to L_{D0} . For immiscible fluid pairs, the diameter ε remains near ε_0 in the threading regime and viscous filaments display traveling varicose deformations in the jetting regime as well as enlargement due to lubrication failure resulting from dynamic partial wetting. The behavior of the detachment length L_D with immiscible fluids decreases with Q_T and tends toward L_{D0} , which is in opposite trend compared to that of miscible fluid pairs since in this situation L_D increases with Q_T . Therefore, our analytical approach based on direct measurement of flow features as a function of control parameters, Q_1 and Q_2 , clearly delineates different phenomena between miscible and immiscible fluid pairs. The method that consists in independently examining the influence of the relative flow rate $\varphi = Q_1/Q_2$ and the absolute flow rate $Q_T = Q_1 + Q_2$ on thread behavior is particularly useful for highlighting similarities and disparities between miscible and immiscible fluids in the absence of a specific conceptual framework. In turn, the development of simple functional relationships based on φ and Q_T facilitates the introduction of dimensionless numbers, such as capillary number Ca and Péclet number Pe , which are useful for conducting similitude studies across fluid pairs and for determining interfacial tension γ_{12} for immiscible fluids and diffusion coefficient D_{12} for miscible fluids depending on microflow regimes of viscous threads. For miscible fluids, the winged regime presents intriguing features for large Q_1 with the presence of recirculating islands suggesting partial miscibility of our silicone oil and polar organic solvents. The winged regime displays intermediate features between diffusive and bulging regimes. Indeed, many thread flow regimes share common characteristics and our extended study of bulk and outer regions of flow maps sheds light on a wealth of interrelated viscous fluid phenomena in confined microsystems. The definition of a viscous regime in the context of microscale flows, however, provides a useful reference for investigating other regimes, including diffusive, capillary, inertial, and gravitational. In each regime, our study underscores the presence of numerous subregimes, such as engulfment, threading, tubing, and bulging within the viscous regime; dripping, jetting, and wetting in the capillary regime; and winged, ultradiffusive, or diffusive buckling in the diffusive regime. Other regimes, such as fragmentation for miscible threads, can be found at low φ and large Q_T , suggesting a possible role of inertia, which is beyond the scope of the present work. Further studies, including theoretical and numerical investigations, would facilitate quantification of complex interactions between flows and fluid physicochemical properties in microchannels. Overall, this work shows the possibility to systematically investigate interfacial flow phenomena with viscous fluids at ultralow interfacial tension using microchannels, which hints at the possible development of microscale hydrodynamic methods for examining spontaneous emulsification between various oils and polar organic solvents in confined microsystems.

ACKNOWLEDGMENT

This material is based upon work supported by the National Science Foundation under Grant No. CBET-1150389.

-
- [1] R. G. Larson, *The Structure and Rheology of Complex Fluids* (Oxford University Press, Inc., New York, 1999).
 - [2] P. Gateau, I. Hénaud, L. Barré, and J. F. Argillier, Heavy oil dilution, *Oil Gas Sci. Technol.* **59**, 503 (2004).
 - [3] A. Aiyejina, D. P. Chakrabarti, A. Pilgrim, and M. K. S. Sastry, Wax formation in oil pipelines: A critical review, *Int. J. Multiphase Flow* **37**, 671 (2011).
 - [4] F. Leal-Calderon, V. Schmitt, and J. Bibette, *Emulsion Science: Basic Principles* (Springer, New York, 2007).
 - [5] D. Klein, *Organic Chemistry* (John Wiley & Sons, Inc., Hoboken, NJ, 2012).
 - [6] G. W. Castellan, *Physical Chemistry* (Addison-Wesley Publishing Company, Reading, MA, 1983).

- [7] A. W. Adamson and A. P. Gast, *Physical Chemistry of Surfaces* (John Wiley & Sons, Inc., New York, 1991).
- [8] N. Shahidzadeh, D. Bonn, J. Meunier, M. Nabavi, M. Airiau, and M. Morvan, Dynamics of spontaneous emulsification for fabrication of oil in water emulsions, *Langmuir* **16**, 9703 (2000).
- [9] S. A. Vitale and J. L. Katz, Liquid droplet dispersions formed by homogeneous liquid-liquid nucleation: “The ouzo effect”, *Langmuir* **19**, 4105 (2003).
- [10] C. A. Miller, Spontaneous emulsification produced by diffusion—a review, *Colloids Surf.* **29**, 89 (1988).
- [11] C. Solans, D. Morales, and M. Homs, Spontaneous emulsification, *Curr. Opin. Colloids Interface Sci.* **22**, 88 (2016).
- [12] T. Cubaud, Swelling of Diffusive Fluid Threads in Microchannels, *Phys. Rev. Lett.* **125**, 174502 (2020).
- [13] R. Hajian and S. Hardt, Formation and lateral migration of nanodroplets via solvent shifting in a microfluidic device, *Microfluid. Nanofluid.* **19**, 1281 (2015).
- [14] H. M. Xia, J. W. Wu, J. J. Zheng, J. Zhang, and Z. P. Wang, Nonlinear microfluidics: Device physics, functions, and applications, *Lab Chip* **21**, 1241 (2021).
- [15] X. Hu and T. Cubaud, Viscous Wave Breaking and Ligament Formation in Microfluidic Systems, *Phys. Rev. Lett.* **121**, 044502 (2018).
- [16] A. Bouchaudy, C. Loussert, and J.-B. Salmon, Steady microfluidic measurements of mutual diffusion coefficients of liquid binary mixtures, *AIChE J.* **64**, 358 (2018).
- [17] W. Li, Z. Nie, H. Zhang, C. Paquet, M. Seo, P. Garstecki, and E. Kumacheva, Screening of the effect of surface energy of microchannels on microfluidic emulsification, *Langmuir* **23**, 8010 (2007).
- [18] P. Poesio, G. P. Beretta, and T. Thorsen, Dissolution of a Liquid Microdroplet in a Nonideal Liquid-Liquid Mixture Far from Thermodynamic Equilibrium, *Phys. Rev. Lett.* **103**, 064501 (2009).
- [19] M. Sauzade and T. Cubaud, Initial microfluidic dissolution regime of CO₂ bubbles in viscous oils, *Phys. Rev. E* **88**, 051001(R) (2013).
- [20] M. S. N. Oliveira, F. T. Pinho, and M. A. Alves, Divergent streamlines and free vortices in Newtonian fluid flows in microfluidic flow-focusing devices, *J. Fluid Mech.* **711**, 171 (2012).
- [21] I. R. Damian, S. Hardt, and C. Balan, From flow focusing to vortex formation in crossing microchannels, *Microfluid. Nanofluid.* **21**, 142 (2017).
- [22] I. Bihi, D. Vesperini, B. Kaoui, and A. Le Goff, Pressure-driven flow focusing of two miscible liquids, *Phys. Fluids* **31**, 062001 (2019).
- [23] K. Doufène, C. Tourné-Péteilh, P. Etienne, and A. Aubert-Pouëssel, Microfluidic systems for droplet generation in aqueous continuous phases: A focus review, *Langmuir* **35**, 12597 (2019).
- [24] G. Bolognesi, A. Hargreaves, A. D. Ward, A. K. Kirby, C. D. Brain, and O. Ces, Microfluidic generation of monodisperse ultra-low interfacial tension oil droplets in water, *RSC Adv.* **5**, 8114 (2015).
- [25] M. Moiré, Y. Peysson, B. Herzhaft, N. Pannacci, F. Gallaire, L. Augello, C. Dalmazzone, and A. Colin, Ultralow interfacial tension measurement through jetting/dripping transition, *Langmuir* **33**, 2531 (2017).
- [26] J. M. Montanero and A. M. Gañán-Calvo, Dripping, jetting and tip streaming, *Rep. Prog. Phys.* **83**, 097001 (2020).
- [27] S. L. Anna, Droplets and bubbles in microfluidic devices, *Annu. Rev. Fluid Mech.* **48**, 285 (2016).
- [28] X. Chen and C. L. Ren, Experimental study on droplet generation in flow focusing devices considering a stratified flow with viscosity contrast, *Chem. Eng. Sci.* **163**, 1 (2017).
- [29] A. Günther and K. F. Jensen, Multiphase microfluidics: From flow characteristics to chemical and material synthesis, *Lab Chip* **6**, 1487 (2006).
- [30] O. du Roure, A. Lindner, E. N. Nazockdast, and M. J. Shelley, Dynamics of flexible fibers in viscous flows and fluids, *Ann. Rev. Fluid Mech.* **51**, 539 (2019).
- [31] N. Mittal, F. Ansari, K. Gowda, C. Brouzet, P. Chen, P. T. Larsson, S. V. Roth, F. Lundell, L. Wågberg, N. A. Kotov *et al.*, Multiscale control of nanocellulose assembly: Transferring remarkable nanoscale fibril mechanics to macroscale fibers, *ACS Nano* **12**, 6378 (2018).
- [32] S. A. Khan and S. Duraiswamy, Microfluidic emulsions with dynamic compound drops, *Lab Chip* **9**, 1840 (2009).

-
- [33] L. L. A. Adams, T. E. Kodger, S.-H. Kim, H. C. Shum, T. Franke, and D. A. Weitz, Single step emulsification for the generation of multi-component double emulsions, *Soft Matter* **8**, 10719 (2012).
- [34] T. J. Ober, D. Foresti, and J. A. Lewis, Active mixing of complex fluids at the microscale, *Proc. Natl. Acad. Sci. USA* **112**, 12293 (2015).
- [35] T. Cubaud, Segmented flows of viscous threads in microchannels, *Phys. Rev. Fluids* **4**, 084201 (2019).
- [36] B. Selvam, S. Merk, R. Govindarajan, and E. Meiburg, Stability of miscible core-annular flows with viscosity stratification, *J. Fluid. Mech.* **592**, 23 (2007).
- [37] D. D. Joseph and Y. Y. Renardy, *Fundamentals of Two-Fluid Dynamics. Part II: Lubricated Transport, Drops and Miscible Liquids* (Springer-Verlag, New York, 1993).
- [38] T. Cubaud and T. G. Mason, High-viscosity fluid threads in weakly diffusive microfluidic systems, *New J. Phys.* **11**, 075029 (2009).
- [39] V. Jayaprakash, M. Costalonga, S. Dhulipala, and K. K. Varanasi, Enhancing the injectability of high concentration drug formulations using core annular flows, *Adv. Healthcare Mater.* **9**, 2001022 (2020).
- [40] P. Dunne *et al.*, Liquid flow and control without solid walls, *Nature (London, UK)* **581**, 58 (2020).
- [41] T. Cubaud and S. Notaro, Regimes of miscible fluid thread formation in microfluidic focusing sections, *Phys. Fluids* **26**, 122005 (2014).
- [42] T. Cubaud and T. G. Mason, Capillary threads and viscous droplets in square microchannels, *Phys. Fluids* **20**, 053302 (2008).
- [43] J. A. Pojman, C. Whitmore, M. L. Turco Liveri, R. Lombardo, J. Marszalek, R. Parker, and B. Zoltowski, Evidence for the existence of an effective interfacial tension between miscible fluids: Isobutyric acid–water and 1-butanol–water in a spinning-drop tensiometer, *Langmuir* **22**, 2569 (2006).
- [44] D. Truzzolillo and L. Cipelletti, Off-equilibrium surface tension in miscible fluids, *Soft Matter* **13**, 13 (2017).
- [45] K. Gowda, C. Brouzet, T. Lefranc, L. D. Söderberg, and F. Lundell, Effective interfacial tension in flow-focusing of colloidal dispersions: 3-D numerical simulations and experiments, *J. Fluid Mech.* **876**, 1052 (2019).
- [46] A. Carbonaro, L. Cipelletti, and D. Truzzolillo, Ultralow effective interfacial tension between miscible molecular fluids, *Phys. Rev. Fluids* **5**, 074001 (2020).
- [47] D. Truzzolillo and L. Cipelletti, Hydrodynamic instabilities in miscible fluids, *J. Phys.: Condens. Matter* **30**, 033001 (2018).
- [48] C. Redon, F. Brochard-Wyart, and F. Rondelez, Dynamics of Dewetting, *Phys. Rev. Lett.* **66**, 715 (1991).
- [49] M. J. Madou, *Fundamentals of Microfabrication and Nanotechnology* (CRC Press, Boca Raton, FL, 2012), Vol II.
- [50] X. Hu and T. Cubaud, Inertial destabilization of highly viscous microfluidic stratifications, *Phys. Rev. Fluids* **1**, 044101 (2016).